Morphology prediction of block copolymers for drug delivery by mesoscale simulations

Paola Posocco, Maurizio Fermeglia and Sabrina Pricl*

Received 3rd May 2010, Accepted 13th June 2010
DOI: 10.1039/c0jm01301c

Polymeric drug carriers have traditionally been considered important for enhancing drug stability and solubility, and improving transport properties of pharmaceutical molecules. Two polymers extensively studied in this regard are poly(lactide) (PLA) and poly(ethylene oxide) (PEO). Nonetheless, a systematic investigation of the main structural and physical factors influencing the ultimate morphology and structure of these block polymer nanoscopic aggregates is still lacking. In this work we report the results of a complete study on the self-assembly of (D-L)-PLA/PEO di/triblock copolymers in aqueous environment and in the presence of a model drug based on a molecular simulation recipe. In detail, atomistic molecular dynamics simulations were used to obtain dissipative particle dynamics (DPD) input parameters, and this mesoscale technique was employed to derive the entire phase diagrams for these systems. Scaling laws for micellar dimensions were applied, and micellar characteristics (*e.g.*, aggregation number) were derived accordingly. The effect of drug-loading on the nanocarrier aggregated morphology was also investigated.

Introduction

Despite remarkable progress in the past century, acute and chronic maladies such as bacterial and viral infections, cancer, cardiovascular disease, and strongly debilitating central nervous system afflictions continue to take a significant toll around the world. Various types of drugs and gene therapy strategies are currently employed for the treatment of diseases based on differences between the normal and pathological tissues. These differences can be subtle and in remote areas of the body at the organ, tissue, cell, or sub-cellular levels. As pathological knowledge is leading to the molecular distinction between normal and abnormal tissue, it is predicted that more therapeutic targets will emerge at all these levels. However, the use of a specific carrier system that can overcome biological barriers and provide optimum drug concentration at the disease target at each level is required.

Nanoscale drug delivery systems – or nanovectors – are ideal candidates to provide essential solutions to the time-honored problem of optimizing the therapeutic index for a treatment (*i.e.*, to maximize efficacy while reducing health-adverse side effects).[1] Three main aspects neatly summarize the essential breakthrough opportunities for nanovector delivery; (i) selective cells and tissue targeting; (ii) ability to reach disease sites where the target cells and tissues are located, and (iii) capacity to deliver even multiple active agents on site. The use of nanoparticle-based pharmaceutical carriers has well established itself over the past decade both in the pharmaceutical research and clinical settings. Nonetheless, many issues are yet to be solved before one new such material can reach the stage of clinical routine.

MOSE-DMNR, University of Trieste, Piazzale Europa 1, 34127 Trieste, Italy. E-mail: sabrina.pricl@dicamp.units.it; Fax: +39 040 569823; Tel: +39 040 5583750

Soft materials, which have characteristic fluid-like disorder on short scale and high order at longer length scale, are increasingly drawing the attention of both scientists and engineers as possible nanocarriers systems. Much of the interest in soft matter, which includes colloids, surfactants, membranes, (bio)polymers and their composites, stems from the inherent capacity for many of these materials to self-assemble into nanostructures. Self-organization is a powerful mean to fabricate useful nanostructured materials and is currently heavily exploited by nature in many of its systems.[2] From the standpoint of pharmaceutical technology, whose main goal is the design of technologically optimal vehicles for the administration of drugs, self-assembly represents a low-cost, fast, and easily scalable process.

Among the plethora of polymeric systems with promising potential as nanoscale drug delivery systems,[3] block copolymers (BCPs) have been widely studied as long-circulating carrier for hydrophobic drugs. BCPs are composed of two or more chemically distinct, and most frequently immiscible, polymer blocks covalently bound together. In the myriad of ways in which blocks can be linked to one another, the simplest and most widely employed categories so far are the *AB* diblock copolymers – composed of a linear chain of type *A* monomers bound to one end to a linear chain of type *B* monomers – and the *ABA* triblock copolymers, in which a linear chain of type *B* monomers is bound to both ends to a linear chain of type *A* monomers (see Scheme 1 (left)). Thermodynamic incompatibility between the *A* and *B* blocks drives a collection of *AB* or *ABA* copolymers to self-organize *via* microphase separation in which the contacts between like and unlike entities tends to be maximized and minimized, respectively. Macrophase separation is prevented by entropic forces stemming from the covalent bonds between the *A*- and *B*-blocks, and the system ultimately reaches a compromise between mixing and separation. The tendency for microphase segregation and the free energy cost of bringing into contact unlike monomers are accounted for by the corresponding values

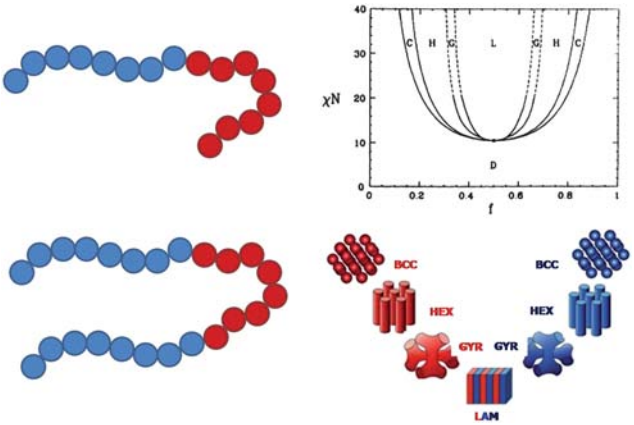

Scheme 1 (left) A schematic representation of the *AB* (top) and *ABA* (bottom) architecture of block copolymers. *A*-type monomers are depicted as light blue spheres, whilst *B*-type monomers are shown as red spheres. Note that in the particular *AB* type copolymer shown as example, the *A*-block length is equal to the *B*-block length. In such case the copolymer is symmetric, and $f_A = f_B = 1/2$. In the case of the illustrated triblock copolymer *ABA*, the fraction of *A*-type monomer is double with respect to that of *B*-type monomers, that is $f_A = 0.67$ and $f_B = 0.33$ (see text for more details). (right) A representative phase diagram for conformationally symmetric diblock melts (top) and cartoon of the corresponding microphase-segregated copolymer morphologies (bottom). Phases are labeled as follows: L/LAM (lamellar), G/GYR (gyroid), H/HEX (hexagonal cylinders), C/BCC (spheres), D (disordered). Dashed lines denote extrapolated phase boundaries, and the dot denotes the critical point.

of the well known temperature-dependent Flory–Huggins parameter χ_{AB}.[4] Two additional parameters concur to determine the ultimate morphology of a microphase segregated copolymer system: the overall degree of polymerization N, and the relative composition fractions, f_A and f_B, where $f_A = N_A/N$ and $f_A + f_B = 1$. In the case of a triblock copolymer *ABA*, a further parameter, *i.e.*, the relative length of the three blocks, must also be considered.

Even in the simplest case, *i.e.*, *AB* diblock copolymers in bulk, a rich assortment of ordered phases has been documented (see Scheme 1 (right)).[4] For nearly symmetric diblocks ($f_A = f_B = 1/2$), a lamellar (L) phase occurs. For moderate asymmetries, a complex bicontinuous state, known as the gyroid (G) phase, has been observed in which the minority blocks form domains consisting of two interweaving threefold-coordinated lattices. Another complex structure, the perforated lamellar (PL) phase, may occur when the minority-component layers of the L phase develop a hexagonal arrangement of passages. At yet higher asymmetries, the minority component forms hexagonally packed cylinders (C) and then spheres (S) arranged on a body-centered cubic lattice. Eventually, as $f \rightarrow 0$ or 1, a disordered phase results. When a solvent component is added to the melt, and in particular if the solvent is selective for one of the copolymer blocks, the resulting system can have an extremely complicated phase diagram that may differ entirely from that of the pure melt. For instance, other phases, which include the micellar phase (M), usually appear. On the other hand, if the solvent is a good solvent of roughly equal affinity for all of the blocks, one can expect that the copolymer system will have thermodynamics similar to that of the pure melt.

Poly(D-L lactide) (PLA) and poly(ethylene oxide) (PEO) are two polymers which have both been extensively investigated for applications as drug delivery systems (DDSs). Both are biodegradable, biocompatible, adapt well to biological environments, and do not have severe adverse effects on blood and tissues. Due to such unique properties, copolymers of PEO/PLA with an *AB* and *ABA* architecture have generated broad interest for use in biomedical applications.[5] Also, depending on the volume ratio between the less soluble (PLA) and soluble (PEO) blocks (the so-called insoluble soluble ratio (ISR)) and independently of whether the different hydrophilic and hydrophobic parts are arranged as *AB* or *ABA*, these copolymer are expected to generate the entire collection of allowed microstructures – spheres, cylinders, lamellas up to micelles – as a result of balancing the different interactions between the two block types and the solvent.

Thermodynamically and kinetically stable copolymeric microstructures, even when encapsulating an active payload, may retain their integrity in the biological environment for long periods and, more effectively, avoid uptake by the reticuloendothelial system (RES) and elimination through the kidney and possibly change the normal organ distribution of an encapsulated drug the same way. At the same time, it can be easily conceived that different microstructures can result in quite diverse nanostructures which, in turn, can perform rather differently in terms of, for instance, drug loading capacity, cellular localization and uptake, cargo release efficiency, and toxicity. The *a priori* knowledge of the phase diagram of a given di/triblock copolymer-based nanocarrier, in particular in the presence of water and/or of an active principle, would therefore constitute an invaluable piece of information in the process development of these DDSs.

For this purpose, it is essential to develop theoretical and computational approaches sufficiently fast and accurate that the structure and property of the materials can be predicted for various conditions. A particular advantage of molecular simulation techniques is that the properties of new materials can be predicted in advance of experiments. This allows the system to be adjusted and refined (or designed) so as to obtain the optimal properties before the arduous experimental task of synthesis and characterization. However, there are significant challenges in using theory to predict accurate properties for nanoscale materials, especially when (bio)macromolecules are involved. Indeed, despite the tremendous advances made in molecular modeling and simulation techniques, there remains a remarkable uncertainty about how to predict many critical properties related to material final performance. The main problem lies in the fact that most of these properties depend on the interactions and chemistry taking place at the atomic level, involving electronic and atomic descriptions at the level of nanometres in the length scale, and picoseconds in the timescale. Conversely, the pharmaceutical technology designer needs answers from microscopic modeling of components having scales of the order of tens/hundreds of nanometres, and of phenomena taking place in a time range of milliseconds or much larger. Thus, to achieve a dramatic advancement in the skill of designing innovative, highly-performing materials, it is mandatory that we link the atomistic to the microscopic modeling.

Molecular modeling and simulation combine methods that cover a range of size scales in order to study material systems. All

together, quantum mechanics (QM), molecular mechanics (MM), molecular dynamics (MD) and Monte Carlo (MC) methods, and mesoscale (MS) techniques cover many decades of both length and time scale, and can be applied to arbitrary materials: solids, liquids, interfaces, self-assembling fluids, gas phase molecules and liquid crystals, to name but a few.[6] There are a number of factors, however, which need to be taken care of to ensure that these methods can be applied routinely and successfully. First and foremost of course are the validity and usability of each method on its own, followed by their interoperability in a common and efficient user environment. Of equal importance is the integration of the simulation methods with experiment. Different-scale simulation can be defined as the enabling technology of science and engineering that links phenomena, models, and information between various scales of complex systems. The idea of many-scale modeling is straightforward: one computes information at a smaller (finer) scale and passes it to a model at a larger (coarser) scale by leaving out (*i.e.*, coarse-graining) degrees of freedom. The ultimate goal of many-scale modeling is then to predict the macroscopic behavior of a chemico-physical process from first principles, *i.e.*, starting from the quantum scale and passing information into molecular scales and eventually to process scales. The MD level allows prediction of the structures and properties for systems much larger in terms of number of atoms than for QM, allowing direct simulations for the properties of many interesting systems. This leads to many relevant and useful results in materials design; however, many critical problems in this field still require time and length scales far too large for practical MD. Hence, the need to model the system at the mesoscale (a scale between the atomistic and the macroscopic) using information retrieved at the atomistic (lower) scale.

This linking through the mesoscale in which the microstructure can be described over a length scale of tens to hundred nanometres is probably the greatest challenge to develop reliable first principles method for practical material design applications.[6] Only by establishing this connection from atomistic to mesoscale it is possible to build a first principles method for describing the properties of new materials. The problem here is that the methods of coarsening the description from atomistic to mesoscale is not as obvious as it is going from electrons to atoms. For example, the strategy for polymers seems quite different from that applicable to metals, which in turn differs from those employed in the case of ceramics or semiconductors. In other words, the coarsening from QM to MD relies on basic principles and can be easily generalized in a method and in a procedure, while the coarsening at higher scales is more system specific for polymer materials due to the larger range of length and time scales that characterize macromolecules.

Scale integration in specific contexts in the field of polymer modeling can be done in different ways. Any 'recipe' for passing information from one scale to another (upper) scale is based on the proper definition of many-scale modeling which consider 'objects' that are relevant at that particular scale, disregard all degrees of freedom of smaller scales, and summarize those degrees of freedom by some representative parameters. As mentioned above, mesoscopic simulations are performed using a coarse-grained molecular model: the particle in mesoscopic simulation is related to a group of several atoms in the atomistic simulation. Dissipative particle dynamics (DPD)[7] is one of the best established mesoscopic simulation techniques, according to which a set of particles moves according to Newton's equation of motion, and interacts dissipatively through simplified force laws. In the DPD model, individual atoms or molecules are not represented directly by the particle, but they are coarse-grained into beads. These beads represent local "fluid packages" able to move independently. DPD thus offers an approach that can be used for modeling physical phenomena occurring at larger time and spatial scales than some other coarse-grained methods as it utilizes a momentum-conserving thermostat and soft repulsive interactions between the beads representing clusters of atoms/molecules. In their seminal work of 1997,[7c] Groot and Warren made a fundamental contribution to this method by establishing a relationship between the main parameter in DPD a_{ij}, *i.e.*, the maximum repulsion between beads of different material type i and j, and the Flory-Huggins parameter χ_{ij}.

In this work we present the results obtained from the application of an atomistic/mesoscale simulation procedure to the prediction of the phase diagrams of racemic PLA and PEO copolymers characterized by *AB* and *ABA* architectures in the presence of water. It is important to observe here the choice of the poly(D-L lactide) instead of one of the two pure enantiomeric blocks (L or D), as it has recently been verified that DDSs in which the *ABA* copolymers contain a racemic mixture of D- and L-lactide are characterized by amorphous PLA domains.[5b] This, in turn, results into systems with different, more tunable drug delivery behavior. Also, as a proof-of-concept demonstration of the utility of these techniques in the formulation of structure–activity relationships for these DDSs, the self-assembly and microsphere formation of PLA-PEO and PLA-PEO-PLA carriers and a model drug (Nifedipine, a poorly soluble drug widely used as calcium channel blocker) under defined compositions is presented and discussed. The DPD method is adopted as the mesoscale modeling technique, and all necessary parameters of the mesoscopic model are estimated by a two-step procedure involving i) the matching of the atomistic and mesoscopic pair correlation functions to determine the best mesoscopic topology for polymers, and ii) the estimation of the DPD interaction parameters *via* the χ_{ij} values obtained from atomistic molecular dynamics simulations, as described below.

Results and discussion

PLA-PEO diblock copolymers

The entire phase diagram of aggregate morphology for the PLA-PEO copolymer with *AB* architecture as a function of the PLA fraction f_{PLA} in the copolymer is shown in Fig. 1. Corresponding to distinctly different structures and morphologies of the aggregates, the diagram is divided into nine, well defined regions. The first one, spanning the entire range of f_{PLA} and a copolymer concentration in water Φ up to ~0.2 v/v is characterized by the presence of micelles, in which the interior core is constituted by the hydrophobic portion of the copolymer (PLA) and the outer corona is decorated by the hydrophilic PEO blocks (*vide infra*). Interestingly, such morphology (particularly important in the formulation of DDSs) is predicted to exist at all Φ values for f_{PLA} up to about 0.1. Moving along the f_{PLA}-axis, as the copolymer

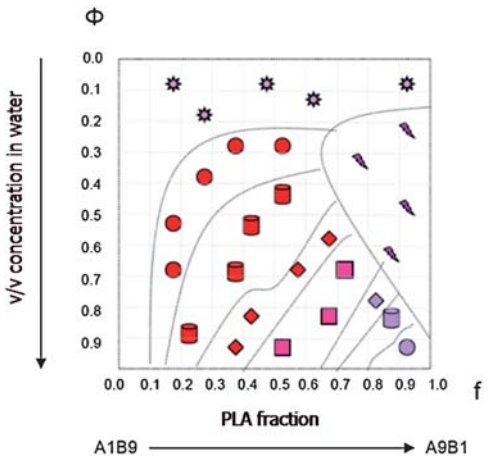

Fig. 1 Phase diagram of the PLA-PEO diblock copolymer of *AB* architecture in water as obtained from the application of the molecular simulation procedure developed in this study. Symbol legend: ⚙, micelles; ●, PLA, spheres; ●, PEO spheres; ▮, PLA cylinders; ▮, PEO cylinders; ◆, PLA perforated lamellas or gyroid phase; ■, lamellas; ◆, PEO perforated lamellas or gyroid phase; ◣, disordered phase. Phase boundary lines are intended only as eye-guidelines.

concentration Φ increases above ~0.3 v/v, the correct sequence of phases is predicted progressively: PLA spheres (BCC), PLA cylinders (HEX), and the PLA gyroid phase (GYR). In correspondence of $f_{PLA} = 0.5$, the phase diagram displays the appearance of the lamellar phase, typical of symmetrical diblock copolymers which, depending on Φ, can persist up to $f_{PLA} = 0.8$. Finally, the right-hand side of the phase diagram shows the region of existence of the reverse-phase morphologies, in the order: PEO GYR, PEO HEX, and PEO BCC, as expected. Interestingly, the ninth region in this phase diagram pertains to what it is usually defined a disordered phase, that is a system for which no canonical or well defined structures can be identified.

Fig. 2 and 3 show a selection of pictorial evidences for each of the phases described above in the case of a PLA-PEO copolymer of the *AB* type as a function of f_{PLA} and at $\Phi = 0.9$ and 0.2 v/v, respectively.

The formation of micelles is a process that minimizes the free energy of an amphiphilic polymer solution through the formation of ordered structures. The free energy of a micelle is the sum of the free energies of the core (F_{core}), corona (F_{corona}), and interface ($F_{interface}$) between them. By forming micelles, the diblocks are able to lower their free energy, since the insoluble blocks aggregate and thus reduce their interface with the solvent. However, formation of micelles results in extension of the core and corona blocks raising their elestic free energy. As a result, changing the size of the two blocks changes the balance of the free energies and this, in turn, changes the micelle dimensions and, hence, their aggregation number. Focusing attention on the phase diagram region in which the self-assembled system is characterized by a morphology most suitable for drug encapsulation and delivery – *i.e.*, spherical micelles – several theories have been proposed for two extreme cases, where either the core- or the shell-forming blocks dominate the micellar structure.[8] Micelles in which the degree of polymerization for the insoluble block is much smaller that the soluble block (*e.g.*, $f_{PLA} \ll f_{PEO}$) are called *starlike* or *hairy* micelles. In this limit, the micelle

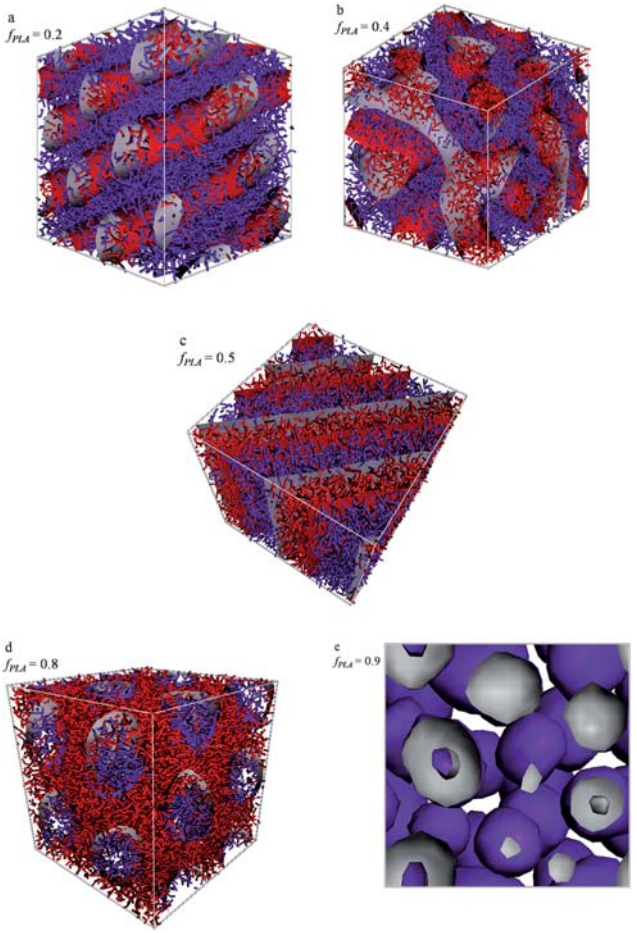

Fig. 2 Predicted phase morphologies for a PLA-PEO diblock copolymer in water at $\Phi = 0.9$ v/v and different f_{PLA} values: (a) $f_{PLA} = 0.2$; (b), $f_{PLA} = 0.4$; (c), $f_{PLA} = 0.5$; (d), $f_{PLA} = 0.8$; (e), $f_{PLA} = 0.9$. Color legend: red, PLA blocks; purple, PEO blocks. Water molecules not displayed for clarity.

consist of a small core of collapsed PLA segments from which PEO chains project to form a large, swollen shell. In the large core limit, (*i.e.*, $f_{PLA} \gg f_{PEO}$), micelles with large insoluble blocks in the cores and short soluble blocks in the coronas are termed *crew-cut* micelles. When studying spherical micelles of either type, there are several parameters which can be identified to characterize the micellar morphology. Among this plethora, the most useful include the overall micellar radius R_m, the core radius R_c, the thickness of the corona H, the aggregation number N_{agg}, and the number density of micelles ζ (*i.e.*, the number of copolymer micelles per unit volume). Taking the PLA-PEO copolymer at $\Phi = 0.2\%$ v/v illustrated in Fig. 3 as a proof-of-concept, all parameters that characterize the relevant micellar associates as extracted from our DPD simulations are reported in Table 1.

The total radius of a micelle is the sum of the radius of the core R_c and the thickness of the corona H. General theory predicts that the individual components R_c and H should exhibit opposite behavior as a function of the degree of polymerization of the insoluble block. Indeed, while the corona thickness should decrease with the degree of polymerization of the insoluble monomer (*e.g.*, f_{PLA}), the core radius is predicted

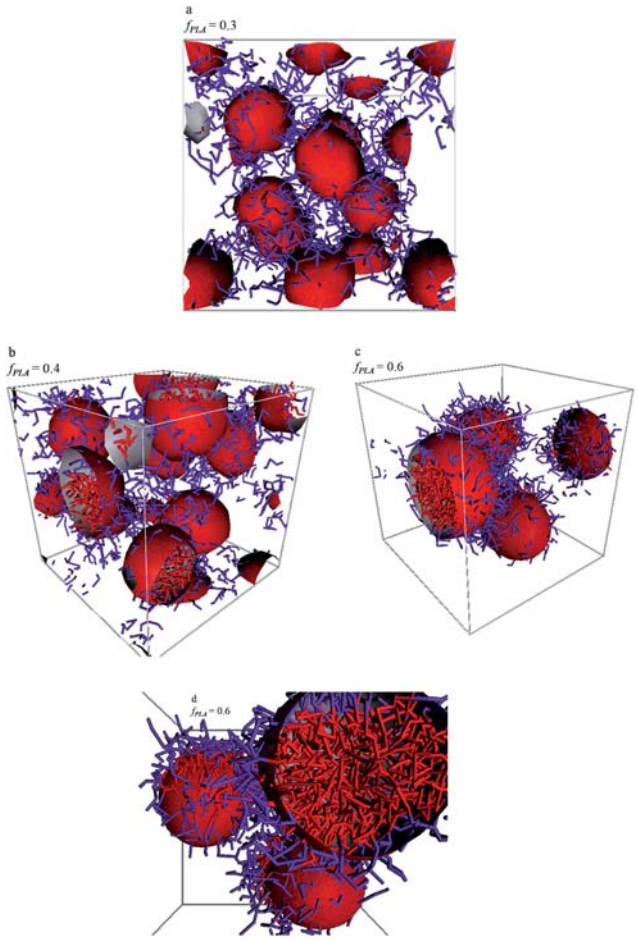

Fig. 3 Predicted phase morphologies for a PLA-PEO diblock copolymer in water at $\Phi = 0.2$ v/v and different f_{PLA} values: (a) $f_{PLA} = 0.3$; (b), $f_{PLA} = 0.4$; (c), $f_{PLA} = 0.6$; (d). Panel (d) is a zoomed in view of the micelles for the system with $f_{PLA} = 0.6$. Color legend: red, PLA blocks; purple, PEO blocks. Water molecules not displayed for clarity.

Table 1 Values of micellar radius R_m (nm), core radius R_c (nm), corona thickness H (nm), aggregation number N_{agg}, micelle number density ζ ($\times 10^{17}$ cm^{-3}), surface area available per copolymer unit at the core/corona interface S_c/N_{agg} (nm^2) and at the outer boundary of the micelle S_t/N_{agg} (nm^2) for the PLA-PEO copolymer at $\Phi = 0.2\%$ v/v in water at different f_{PLA} values

f_{PLA}	R_m	R_c	H	N_{agg}	ζ	S_c/N_{agg}	S_t/N_{agg}
0.1	10.4 ± 0.3	2.79 ± 0.4	7.60	12	17	8	113
0.2	11.6 ± 0.2	4.22 ± 0.3	7.35	21	9.8	11	81
0.3	12.7 ± 0.3	5.39 ± 0.3	7.33	29	7.1	13	70
0.4	13.2 ± 0.3	6.40 ± 0.4	6.79	36	5.6	14	60
0.5	14.8 ± 0.4	9.30 ± 0.5	5.49	80	2.6	14	35
0.6	15.4 ± 0.1	10.5 ± 0.3	4.89	192	1.1	7	16
0.7	15.9 ± 0.3	11.6 ± 0.2	4.30	248	0.83	7	13
0.8	16.4 ± 0.2	12.7 ± 0.2	3.71	289	0.71	7	12
0.9	17.0 ± 0.2	13.8 ± 0.1	3.17	366	0.56	7	10

to increase. The latter prediction is also consistent with an increase of the aggregation number N_{agg} with f_{PLA}, on the (sensible) assumption that the density inside the core remains constant. As can be seen from Table 1, the micelle radius R_m increases with increasing f_{PLA}, and so do R_c and N_{agg}, while H decreases, in harmony with theory. Interestingly, if compared with the corresponding extended (*all trans*) lengths of PLA chains of equal degree of polymerization (calculated to range from 4.6 to 414 nm using the length of a lactic acid unit equal to 4.6 Å as derived from the MD simulations), the mean R_c values are considerably lower. This clearly indicates that, as for many similar AB copolymer architectures in B-selective solvents, the PLA blocks of the PLA-PEO copolymer adopt a rather collapsed conformation in the core. Also, the greater f_{PLA}, and the greater the degree of compactness of the PLA-block within the core. Simple calculations shown that, for instance, the PLA chains in the $f_{PLA} = 0.1$ micellar-like assembly are much more linearly extended (~60% of the fully extended length) than those for which $f_{PLA} = 0.5$ (~40%) or $f_{PLA} = 0.9$ (~33%). This evidence is a direct consequence of the balance between PEO/PEO and PLA/PLA interactions: as f_{PLA} increases, the augmented number of hydrophobic interactions among the PLA segments draw the PEO segments closer to one another (corresponding to a decrease of H), and allow for a more compact arrangement of the PLA monomers is the core.

An overall plot of R_m and R_c as a function of N_{PLA} (not shown) indicates a sharp morphological transition from a starlike to a crew-cut regime for the PLA-PEO copolymer at $\Phi = 0.2\%$ v/v, the cross-over being located at $f_{PLA} = f_{PEO}$ (Fig. 4a). Applying simple scaling concepts,[8] for the hairy micelles R_c and R_m are found to increase with N_{PLA} according to:

$$R_c \approx N_{PLA}^{\frac{3}{5}} a \quad (1)$$

and

$$R_m \approx N_{PLA}^{\frac{4}{25}} N_{PEO}^{\frac{3}{5}} a \quad (2)$$

where a is a typical monomer size (Fig. 4a). In the crew-cut regime, the corona thickness is negligible in comparison to R_m, so that $R_c \sim R_m$ and R_m scales with N_{PLA} as (Fig. 4b):

$$R_m \approx N_{PLA}^{\frac{2}{3}} a \quad (3)$$

The aggregation number N_{agg} for the same PLA-PEO system is also found to scale in the starlike and crew-cut regimes as $N_{agg} \approx N_{PLA}^{\frac{4}{5}}$ and $N_{agg} \approx N_{PLA}$, respectively. Accordingly, for small f_{PLA} values, when the hydrophobic interactions between the low molecular weight PLA chains are weak, the corresponding starlike micelles are expected to form loosely packed micellar assemblies with a lot of solvent within the shell region. On the contrary, when strong, net hydrophobic (enthalpic) interactions between higher molecular weight PLA blocks

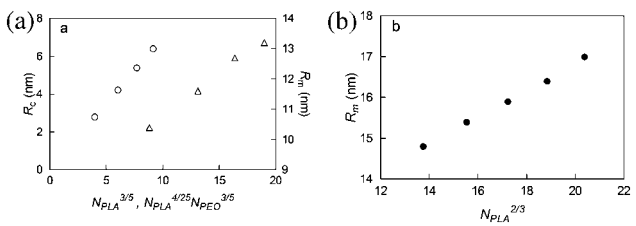

Fig. 4 (a) Scaling behavior of R_c (○, left axis) and R_m (Δ, right axis) in the starlike micelle regime and (b) scaling of R_m (●) in the crew-cut micelle regime a PLA-PEO diblock copolymer in water at $\Phi = 0.2$ v/v.

overcome the repulsive (entropic) forces between neighboring PEO chains in the corona, micelles with large N_{agg} can be formed.

This concept is clearly illustrated by considering the surface area available per copolymer unit at the outer boundary of the micelle (S_t/N_{agg}), and at the core/corona interface (S_c/N_{agg}) (Table 1). S_t/N_{agg} and S_c/N_{agg} can be easily obtained by calculating the external and core surface areas of each micelle as $S_t = 4\pi R_m^2$ and $S_c = 4\pi R_c^2$, respectively, using the values listed in Table 1. Taking the copolymer with the lowest f_{PLA} as an example, the surface area available per PEO block in the micelle is approximately 113 nm^2. This value can be aptly compared to the surface area that would be occupied by a PEO chain of equal molecular weight (*i.e.*, 6336 kDa) in free solution. Resorting to the relationship derived by Devanand and Selser for the radius of gyration R_g of PEO as a function of the molecular weight in a good solvent,[9] a PEO chain of $N_{PEO} = 144$ would be characterized by an R_g value of 3.2 nm. Accordingly, such a chain in free solution would occupy a sphere with a maximum cross-sectional area (πR_g^2) of 32.9 nm^2. If compared to this value, S_t/N_{agg} appears to be very high, implying that the PEO soluble blocks are quite spread out into the solvent with a considerable degree of conformational freedom at the periphery of the micellar corona. As f_{PLA} increases, the number of attractive hydrophobic interactions leads to a tighter association between the PLA blocks in the micelle core. As a consequence, the PLA chains more forcibly draw together the solvated PEO blocks, resulting in a substantial increase of N_{agg} and, hence, a decline in S_t/N_{agg}. The increase of N_{agg} and the concomitant decrease of the surface curvature (*i.e.*, the gradual transition between starlike and crew-cut micelles) result in a considerable reduction of H, and hence of the volume available to each of the PEO chains in the corona. To alleviate entropically unfavorable overlaps upon between overcrowded segments, the PEO chains may then change their conformation from swollen to stretched coils in the outer shell. Finally, in the crew-cut regime, a balance between the growth of N_{agg} and the corresponding increase of R_c and R_m seems to lead to an almost constant value of S_t/N_{agg}.

Similarly, the surface area available per PEO chain at the core/corona interface S_c/N_{agg} increases with f_{PLA}, revealing a higher grafting density for the more hydrophilic copolymers with respect to the more hydrophobic counterparts. However, at all copolymer composition, S_c/N_{agg} remains considerably lower than that pertaining to isolated PEO chains of analogous molecular weight in free solution (*e.g.*, compare the value of 8 nm^2 with 30 nm^2 for the 6336 PEO chain discussed above). This, in turn, means that the PEO hydrophilic blocks in this PLA-PEO copolymer tend to adopt a brushlike configuration.[10] De Gennes scaling theories for grafted polymer brushes predicts that the layer thickness of a grafted polymer brush should exhibit an inverse dependence on the distance between the grafting points.[10] This is indeed the case for the micelles in the starlike regime, with the copolymers having the lowest f_{PLA} being characterized by higher PEO chain grafting density N_{agg}/S_c and, correspondingly, thicker PEO layers H.

As a last, yet very important comment, all micelle morphological parameters obtained for the PLA-PEO system shown in Table 1 are in full agreement with the corresponding experimental values and trends exhibited by closely PLA-PEO diblock copolymer systems in water.[11]

PLA-PEO-PLA triblock copolymers

In the case of the triblock copolymer PLA-PEO-PLA with the linear architecture *ABA* sketched in Scheme 1 (left), the corresponding phase diagram is more complicated, with the

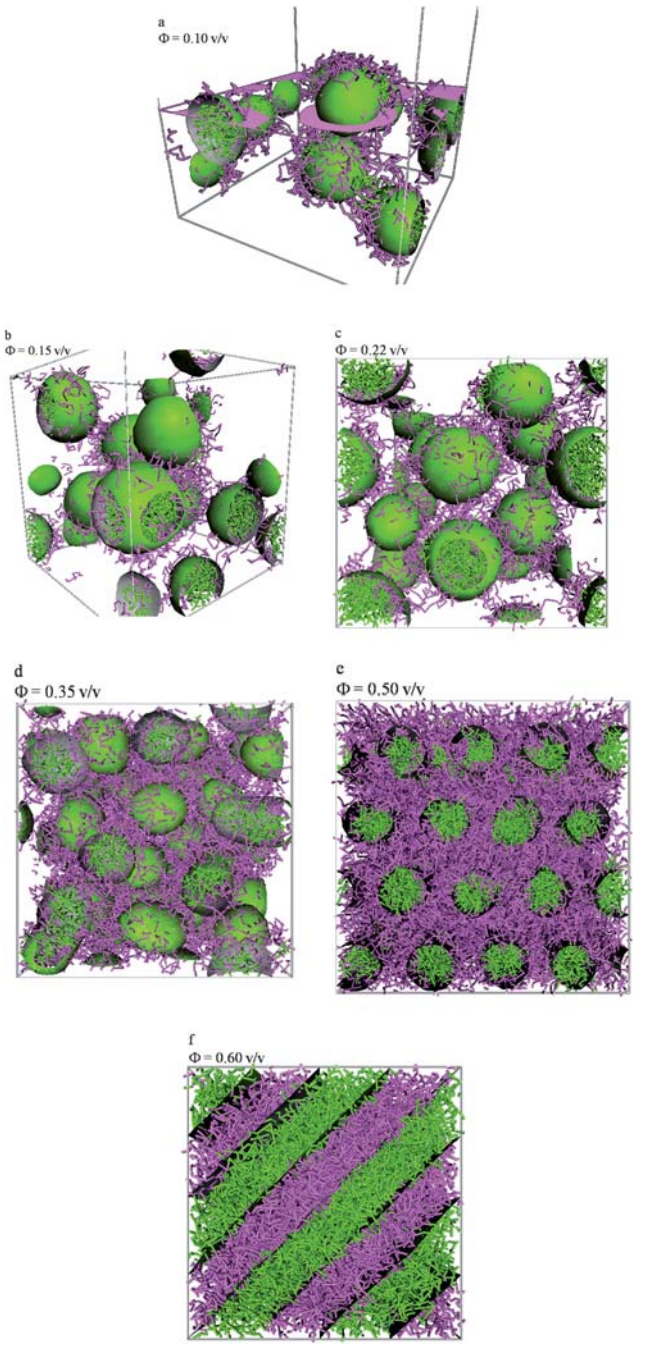

Fig. 5 Predicted phase morphologies for a PLA-PEO-PLA triblock copolymer in water at $f_{PLA} = 0.57$ and different Φ values: (a), $\Phi = 0.1$ v/v; (b), $\Phi = 0.15$ v/v; (c), $\Phi = 0.22$ v/v; (d), $\Phi = 0.35$ v/v; (e), $\Phi = 0.50$ v/v; (f), $\Phi = 0.60$ v/v. Color legend: green, PLA blocks; purple, PEO blocks. Water molecules not displayed for clarity. In panel (a) a cut-plane is highlighted for graphical purposes.

appearance of a hydrogel phase for intermediate values of polymer concentration Φ. As an example, Fig. 5 illustrates the aggregate morphologies obtained from the application of the simulation procedure developed in this work to *ABA* copolymer characterized by an f_{PLA} of 0.57. As can be readily seen from the images, for this system the simulation reveals the existence of well separated micelles, with an inner PLA core surrounded by a corona of the hydrated PEO block only in a narrow range of Φ.

Upon increasing Φ, the transition to a *flowerlike* micellar morphology is observed, which persist up to $\Phi \sim 0.15$ v/v. At still higher values of Φ, bridging between micelles takes place, leading to formation of a three-dimensional network and gelation. The junction points formed are temporary and reversible, and therefore, they break and re-form frequently over the time scale of the simulation. For a polymer concentration of ~ 0.5 the hexagonal geometry characterizes the predicted morphology which, upon further increasing of Φ, undergoes a phase transition to the lamellar one.

Importantly, this predicted behavior is in excellent agreement with the recent experimental results obtained by Agrawal and his group,[5a,b,d,f,g] and thus deserves a deeper comment. In the last of a series of elegant and thorough studies,[5b] these authors have verified that PLA-PEO-PLA triblock copolymers characterized by amorphous PLA domains form spherical micelles at very low concentration in water solution. The end PLA blocks, which are poorly compatible if at all with the solvent, make up the micellar core, whilst the hydrophilic midblock generated the micellar corona (see Fig. 6 (top left panel)). As the polymer concentration increases, the micelles begin to interact by virtue of the intensive

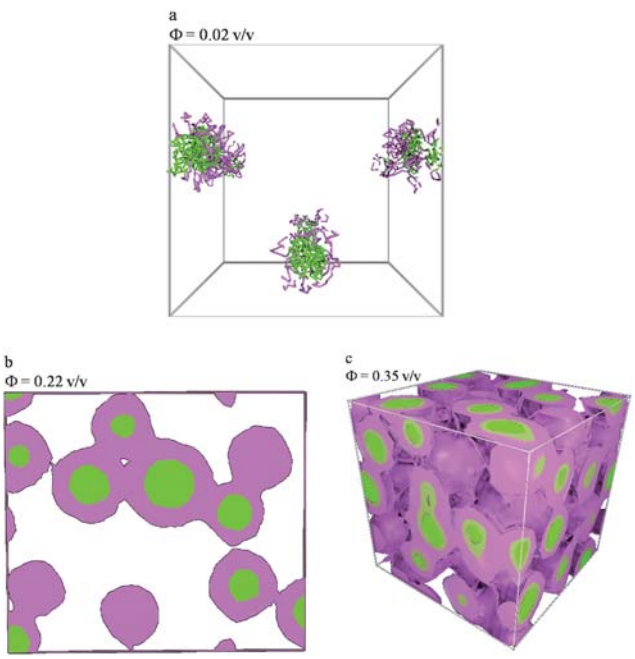

Fig. 6 Evolution of micellar aggregation for the PLA-PEO-PLA copolymer as a function of polymer concentration Φ at constant PLA fraction $f_{PLA} = 0.57$. (a), $\Phi = 0.02$ v/v; (b), $\Phi = 0.22$ v/v; (c), $\Phi = 0.35$ v/v. Color legend: green, PLA blocks; purple, PEO blocks. Water molecules not displayed for clarity. In panel (b) a volume representation in a plane cut along the simulation cell is shown. In panel (c) a three-dimensional volume representation is chosen to highlight the percolating connectivity in the hydrogel.

hydrophobic attraction among the core phases: the intermicellar spacing progressively decreases while the flowerlike micelles become more closely packed and the bridges of PEO blocks among them increase in number (see Fig. 5 (top right panel)). Further increasing the bridging density eventually leads to the point where all micelles are connected into a network in solution, namely the percolation threshold, thereby resulting in the formation of a gel at high concentration (see Fig. 5 (bottom panel)).

Another interesting piece of evidence of a good match between simulated and experimental results stems from the estimation of the micelle dimensions for the PLA-PEO-PLA copolymer. Taking the systems with $\Phi = 0.22$ v/v as a proof of principle, the average estimated values of the micelle PLA core radius R_c as extracted from the DPD simulations is 6.4 ± 0.3 nm whilst the average radius of an entire micelle R_m amounts to 9.7 ± 0.2 nm. Accordingly, the thickness of the PEO shell H is equal to 3.3 nm. These values are in utter agreement with previously reported experimental studies on closely related PLA-PEO-PLA water systems.[5b,11g] Beside the aggregation number discussed above for the AB diblock case, another parameter can be used to further characterize these micellar structures the degree of the hydration shell, φ_{sh}. This quantity can be calculated, at first approximation, using the following relationship:

$$\varphi_{sh} = 1 - \frac{N_{agg} V_{PEO}}{\left(\frac{4}{3\pi\left(R_m^3 - R_c^3\right)}\right)} \quad (4)$$

in which V_{PEO} is the molecular volume of PEO. Applying eqn (4) to the PLA-PEO-PLA systems with $\Phi = 0.22$ v/v as an example, using the estimated value of the aggregation number $N_{agg} = 179$, yields a value for $\varphi_{sh} = 0.32$, again in agreement with the corresponding estimates reported in the literature for analogous systems.[5b,11g] It is worth noting that the substantial value of N_{agg} is in harmony with the morphological evidences that, also for the *ABA* PLA-PEO-PLA copolymers, the big PLA domains tend to be strongly phase-separated in the micellar core and, also, supports that fact that these large segregated hydrophobic domains tend to interact strongly among themselves, ultimately leading to the formation of the micellar network. Under this condition, where the micelles are expected to be densely packed, the center-to-center distance between any two adjacent micelles should in principle be equal to the micelle diameter. This seems to be almost the case for the PLA-PEO-PLA systems with $\Phi = 0.35$ v/v and $f_{PLA} = 0.57$, (see Fig. 5 (center right panel) and 6 (bottom panel)). On the other hand, at lower copolymer concentrations the intermicellar radii are mostly seen to be larger than R_m (see, for example, Fig. 5 (top left and right panels)), indicating that the close-packing condition and, hence, the percolation threshold, is far from being reached for these systems. In passing, we also note that calculated degree of hydration of 32% for the above mentioned system is in line with the expected balance between a good hydration level and the partial engagement of these blocks in bridging the flowerlike micelles through the solution.

Micelle loading with a model drug

To test the ability of the adopted methodology to account for the effect of drug-loading on the nanocarrier aggregated

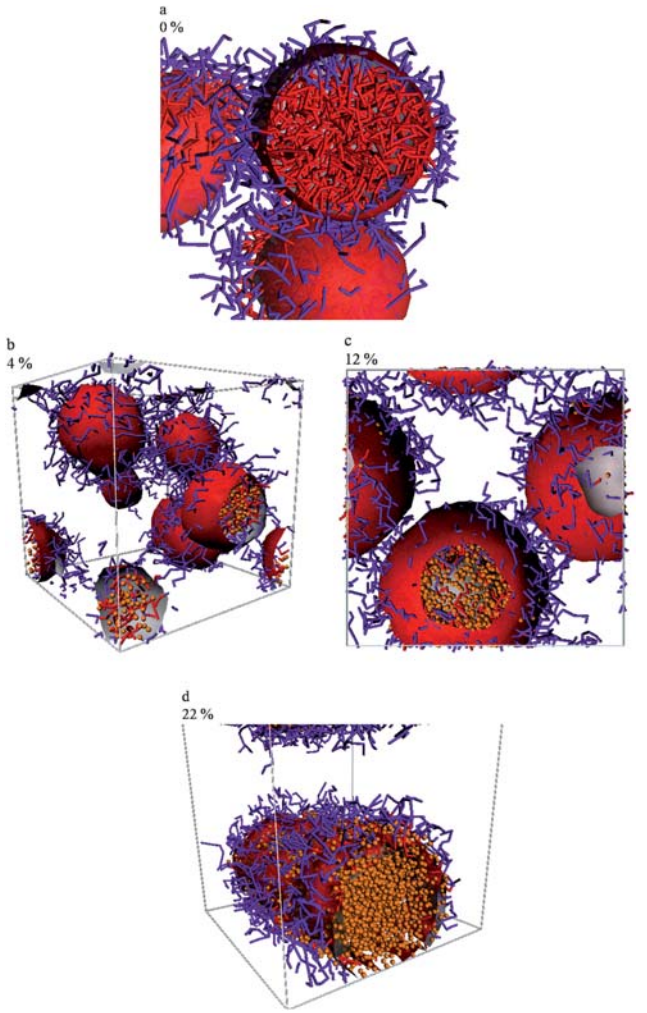

Fig. 7 Evolution of the micellar aggregate morphology for the PLA-PEO copolymer at $\Phi = 0.15$ v/v and $f_{PLA} = 0.3$ as a function of Nifedipine loading (% v/v). (a), no drug loading; (b), 4%; (c), 12%; (d) 22%. Color legend: purple, PEO blocks; red, PLA blocks, orange, drug. Water molecules not displayed for clarity.

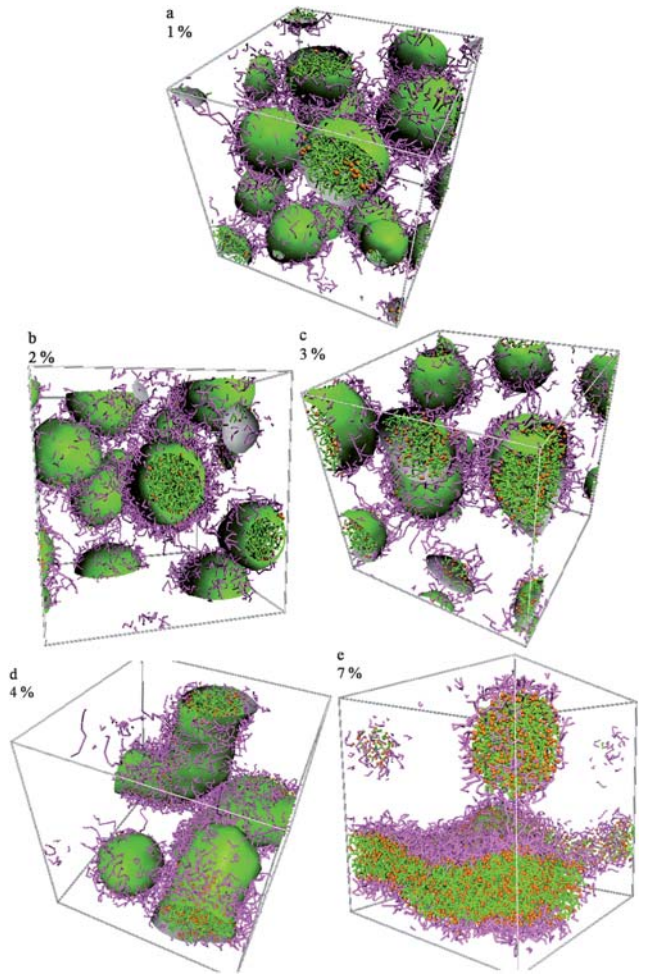

Fig. 8 Evolution of the micellar aggregate morphology for the PLA-PEO-PLA copolymer at $\Phi = 0.22$ v/v and $f_{PLA} = 0.57$ as a function of Nifedipine loading (% v/v). (a), 1%; (b), 2%; (c), 3%, (d) 4%; (e) 7%. Color legend: green, PLA blocks; purple, PEO blocks, orange, drug. Water molecules not displayed for clarity.

morphology, further simulations were performed both on the di- and tri-block copolymer systems containing the model drug Nefidipine in concentration and composition intervals of pharmaceutical technology interest. The first three panels of Fig. 7 show the evolution of the morphology for the system PLA-PEO characterized by $\Phi = 0.15$ v/v and $f_{PLA} = 0.3$ upon different drug loading as an example. As can be seen from these figures, upon addition of the active principle up to ~12% v/v, the micellar morphology, although characterized by bigger dimensions, can still be observed, with the drug fully and well dispersed into the PLA hydrophobic core (Fig. 7 (top right panel)). A further increase in drug loading up to 22% v/v leads to the formation of columnar micelles (Fig. 6 (bottom left panel)). This concentration threshold seems then to mark the maximum payload the considered copolymer nanocarrier can take on under the selected conditions.

Considering now the triblock PLA-PEO-PLA copolymer, an analogous morphology evolution upon drug loading is envisaged. As illustrated in Fig. 8 for the *ABA* copolymer system with $\Phi = 0.22$ v/v and $f_{PLA} = 0.57$ as an example, the nanocarrier is able to accommodate the drug within the PLA core and without an appreciable alteration of the micellar morphology up to a concentration of 3% v/v. At 4% v/v a transition to columnar or wormlike micelles is observed and, finally, in correspondence to a drug load of 7% v/v, the fusion of the micelles into a bilayer membrane is predicted. In other words, as the drug concentration increases, the local packing of the hydrophobic entities (*i.e.*, PLA blocks and drug molecules) changes, and progressively leads to a decrease of the local curvature. Thus, those systems which at low drug concentrations still form spherical aggregates will rearrange their assembly into cylindrical or eventually membrane-like aggregate (consisting of two monolayers of block copolymers aligned so as to form a sandwich-like membrane: soluble block-insoluble block with interspersed drug-soluble blocks) as the payload amount increases.

Conclusions

In this work we report the results of a complete study on the self-assembly of (D-L)-PLA/PEO di/triblock copolymers in aqueous

environment and in the presence of a model drug based on a molecular simulation recipe. In detail, atomistic molecular dynamics simulations were used to obtain dissipative particle dynamics (DPD) input parameters, and this mesoscale technique was employed to derive the entire phase diagrams for these systems. Scaling laws for micellar dimensions were applied, and micellar characteristics such as micellar dimensions, aggregation numbers, micelle number density, and degree of hydration of the outer corona were derived accordingly. Further, the effect of drug-loading on the nanocarrier aggregated morphology was also investigated, highlighting a critical drug payload for each copolymer system.

Novel approaches to drug delivery and formulation using nanotechnology are revolutionizing the future of medicine. At the time of writing, nanomedicine – the medical application of nanotechnology – offers the promise of an endless range of applications from biomedical imaging to drug delivery and therapeutics which, coupled to genomic tailoring, may soon spawn the much-anticipated and highly-pursued individualized medicine. The specific area of nanoformulations includes the creation of many different nanoscale DDSs such as those discussed in the present paper, which can be created from a countless combination of materials and active principles. These nanovectors can be tailored for working in specific tissues or individual patients, and may eliminate the need for conditional administration of drugs, thereby promoting patient compliance and maximizing therapeutic effects.

Being able to formulate an *a priori* quantitative structure-property or structure–activity relationship for a novel nanocarrier in a given solvent and in the eventual presence of a drug cargo – possibly even before the nanoformulation preparation is attempted in the laboratory – would constitute a giant leap towards an advancement in pharmaceutical technology. Time, economical resources, and human efforts could then be minimized and focused on the most promising DDS systems designed on the basis of the application of these computer-assisted QSPRs/QSARs. The procedure and the results presented in this work, based on the application of a multiscale molecular modeling recipe for the phase diagram prediction for block copolymers in water and in the presence of a model drug, represent one example of this grand challenge. Hopefully, the outstanding agreement between predicted and experimental morphologies obtained for these DDSs may pave the way for these *in silico* approaches to become part of the arsenal of techniques used every day in pharmaceutical technology, the only limitation being human creativity.

Computational methodology

Fundamentals of DPD theory

An important concept of dissipative particle dynamics (DPD) simulation[7] is that a number of atoms (or a volume of fluid) is coarse-grained onto a single DPD bead according to their chemical identity and their environment. The beads interact with each other by pairwise additive forces that locally conserve momentum and lead to the correct thermodynamics.[12] A given particle i at position $\boldsymbol{r}_i$ surrounded by particles $j \neq i$ at $\boldsymbol{r}_j$ (distance vector $\boldsymbol{r}_{ij} = \boldsymbol{r}_i - \boldsymbol{r}_j$, and unit vector $\hat{r}_{ij} = \frac{r_{ij}}{|r_{ij}|}$) experience a force with components:

$$f_i = \sum_{i \neq j} \left(F_{ij}^C + F_{ij}^R + F_{ij}^D \right) \tag{5}$$

where the sum runs over all the particles within a cutoff radius r_c. The conservative force F_{ij}^C is a soft repulsive term that act along the line connecting two bead centers, and is given by:

$$F_{ij}^C = f(x) = \begin{cases} a_{ij}\left(1 - \frac{r_{ij}}{r_c}\right)\hat{r}_{ij} & (r_{ij} \geq r_c) \\ 0 & (r_{ij} \geq r_c) \end{cases} \tag{6}$$

where a_{ij} is the maximum repulsion between particles i and j. The second term on the right hand side of eqn (5) is a random force, given by:

$$F_{ij}^R = \frac{\sigma\left(1 - \frac{r_{ij}}{r_c}\right)\hat{r}_{ij}\zeta_{ij}}{\sqrt{dt}} \tag{7}$$

whilst the third represents a dissipative force:

$$F_{ij}^D = -\gamma\left(1 - \frac{r_{ij}}{r_c}\right)^2 (\hat{r}_{ij} \bullet \nu_{ij})\hat{r}_{ij} \tag{8}$$

The velocity-dependent dissipative force F_{ij}^D provides a viscous drag to the particles, whereas the random component F_{ij}^R counteracts the system cooling by applying random kicks to the particles that tend to increase the relative velocities of adjacent pairs. Accordingly, the coupling of F_{ij}^D and F_{ij}^R acts as a thermostat for the DPD particle system. The term ζ_{ij} in eqn (7) is a randomly fluctuating variable that has a Gaussian statistic with a zero mean and a variance of 1. In eqn (8), the relative velocity of two DPD particles $\nu_{ij} = \nu_i - \nu_j$ and the friction coefficient γ are related to the magnitude of the random force σ by $\sigma = 2\gamma k_B T$. The entire set of DPD beads is evolved in time according to Newton's equation of motion. For the sake of simplicity, each bead mass m_i is assumed to be the same and set equal to unity; also, the cutoff radius is set $r_c = 1$, which is the basic unit length of the system. With $k_B T = 1$ defining the unit of energy, the DPD time units then becomes $\tau = r_c\left(\frac{m}{k_B T}\right)^{\frac{1}{2}}$.

As anticipated, DPD particles represent groups of real atoms or polymer monomers; thus, atomistic level details are lost while interactions between different bead types become the main parameters governing the mesoscopic system behavior. The a_{ij} parameter in eqn (6) is the main DPD interaction parameter, with the dimension of a force. As a consequence of the purely repulsive nature of the conservative force F_{ij}^C defining a_{ij}, only liquid–liquid or solid–liquid interfaces can be simulated in constant volume DPD ensembles. In this respect, the DPD theory is similar to the Flory-Huggins therory of lattice polymers and, indeed, the interaction parameter a_{ij} of the DPD conservative force can be mapped onto the Flory-Huggins parameter χ_{ij} by assuming that, for a polymer, the beads are connected in a chain by springs.[7c] Assuming that the interactions for similar beads are equal (*i.e.*, $a_{ii} = a_{jj}$), in this work we used the following relationship recently proposed by Glotzer *et al.*[13] as a modification of the original equation of Groot and Warren[6c] to better account for the polymer chain length to relate χ_{ij} to a_{ij} and a_{ii}:

$$a_{ij} = a_{ii} + 3.27 \times \left(1 + \frac{3.9}{N_{DPD}^{0.51}}\right)\chi_{ij} \quad (9)$$

in which N_{DPD} is the number of DPD beads making up the polymeric chain.

In order to calculate a_{ij}, both a_{ii} and χ_{ij} should be determined. The repulsion parameter between like-particles a_{ii} can be chosen according to[14] $a_{ii}\rho = 75k_BT$. Setting $\rho = 3$ leads to $a_{ii} = 25$.[6c] The Flory-Huggins parameter can, in turn, be estimated from the Hildebrand solubility parameter δ as:

$$\chi_{ij} = \frac{V}{k_BT}(\delta_i - \delta_j)^2 \quad (10)$$

where V is the average volume of the beads i and j, and δ_i and δ_j are the solubility parameters of bead i and j, respectively.

The solubility parameters are material-specific numbers which can be obtained from experiments of simulations. Om this study, we performed atomistic molecular dynamics (MD) simulations to calculate the cohesive energy densities (*CED*) from the nonbonded interaction energies and the molar volumes (*vide infra*). The values of δ for a given species i, δ_i, can then be estimated using the following relationship:

$$\delta_i = \left(\frac{\Delta H_{v,i}}{V_{m,i}}\right)^{\frac{1}{2}} = (CED_i)^{\frac{1}{2}} \quad (11)$$

in which $\Delta H_{v,i}$ is the molar enthalpy of vaporization and $V_{m,i}$ is the molar volume of the molecular species i.

DPD parameter determination

With the purpose of simulating *AB* and *ABA* copolymers of PLA and PEO of practical interest for the pharmaceutical technology, the following macromolecules were chosen as proof-of-concept systems: PLA_xPEO_y with $x = 720$–6480 and $y = 704$–6336 for the diblock, and $PLA_{5875}PEO_{8448}PLA_{5875}$ for the triblock copolymer, respectively.

The first step in the computational recipe applied in this work then consisted in the determination of the coarse-grained models for the PLA and PEO polymers, respectively. Following our previous work on different systems,[6] at first atomistic molecular dynamics (MD) simulations were performed on the di- and triblock copolymer chains. The amorphous polymer models for PEO and (D-L)PLA chains were built with the rotational isomeric state (RIS) method developed by Theodorou and Suter.[15] Each polymeric structure was then relaxed and subjected to our well-validated combined molecular mechanics/molecular dynamics simulated annealing (MDSA) protocol,[16] in which the relaxed molecular structure is subjected to five repeated temperature cycles using constant volume/constant temperature (NVT) MD conditions. At the end of each annealing cycle, the structure is again energy minimized, and only the structure corresponding to the minimum energy is used for further modeling. Each final chain structure was assigned atomic charges using the charge scheme proposed by Li and Goddard.[17] In the generation of the polymer simulation cells, the PCFF force field as modified by Blomqvist *et al.*[18] was employed, as this force field was shown to accurately reproduce the torsional statistics for the dihedral angles of the added bonds of the polymers considered in this study.[19] To obtain sufficient statistics for averaging the computed properties of interest, 10 amorphous cells containing 5 chains with a chain length with a degree of polymerization of 90 and 192 for PLA and PEO, respectively, at a density lower than the corresponding experimental value were built and relaxed *via* an alternation of molecular mechanics (MM) minimization (using the conjugate gradient method) and isochoric-isothermal (NVT) MD equilibration at 600 K to avoid trapping the system in high-energy minima. Typically, 5000 MM and 50000 MD steps (using the Verlet algorithm with an integration step of 1 fs) were employed in one cycle, and 5 to 10 steps were needed to achieve statistically stable configurations. After system relaxation, the densities of the cells were increased to the corresponding experimental values (*i.e.*, 1.07 g cm^{-3} for PEO and 1.25 g cm^{-3} for (D-L)PLA), and 3 ns isobaric-isothermal (NPT) simulations at 308.15 K were performed to equilibrate the system at the proper densities, followed by 5 ns NVT simulations necessary for CED_i and, hence δ_i. and ultimately χ_{ij} calculations according to eqn (10) and (11).[6] A similar procedure was applied to calculate the same quantities for Nefidipine and water.

The coarse-graining of the copolymer atoms into DPD beads were then obtained as follows.[6a,20] Using the equilibrium NVT MD production runs, the pair correlation functions were calculated using the following formula:

$$P_{IJ}(r_Ir_J) = \sum_i \sum_j \theta_{Ii}\theta_{Jj}\big(\delta(r_I - R_i)\delta(r_J - R_j)\big) \quad (12)$$

where the sum runs over all atoms i and j in the molecular fragments I and J, and the square brackets indicate a thermal average. θ_{Ii} is a simple step function defined as:

$$\theta_{Ii}\begin{cases} 1 \text{ if } i \text{ is of type } I \\ 0 \text{ if } i \text{ is not of type } I \end{cases} \quad (13)$$

DPD simulations were then performed for each polymer using a repulsion parameter a_{ij} of 25 for all bead-bead interactions and, similarly to MD, the corresponding pair correlations between the different beads were computed. The optimal overlap of the pair correlation functions obtained from the MD and the coarse-grained models was achieved with 10 PLA monomers and 16 PEO monomers per each PLA and PEO DPD bead, respectively. This mapping in turn resulted in the following mesoscopic copolymer architectures: PLA_nPEO_m with $n + m = 10$ for the *AB* copolymer, and $PLA_8PEO_{12}PLA_8$ for the *ABA* copolymer. Once these models were defined, the basic DPD assumption that all bead-types should be of comparable volume ultimately led to the coarse-graining of the entire molecule of Nefidipine into one DRUG bead, and 48 water molecules in each SOLVENT bead, respectively.

Lastly, the main DPD interaction parameter a_{ij} for all DPD bead types were obtained using the χ_{ij} determined from the MD simulations *via* eqn (9). The values of the resulting interaction parameters a_{ij} for all DPD species defined above and used for the mesoscale simulations are listed in Table 2.

All simulations were performed in a $20^3 \times r_c$ box and in a $30^3 \times r_c$ box for the *AB* and *ABA* systems, respectively. In all cases, including the di(tri)-block copolymer + solvent + drug systems, the DPD simulations started from homogeneously mixed configurations. A density value $\rho = 3$ was considered, and periodic boundary conditions were applied in all directions. The

Table 2 DPD interaction parameters a_{ij} used in the mesoscale simulations

	PLA	PEO	Solvent	Drug
PLA	25	50.2	69.1	25.3
PEO	50.2	25	25	34
SOLVENT	69.1	25	25	66.3
DRUG	25.3	34	66.3	25

dimensionless time step of 0.05 was employed and 10^6 steps have been adopted to get a steady state at a constant temperature of 308.15 K.

Acknowledgements

The financial support from the Ministry of Instruction, University, and Research (MIUR, Rome, Italy) in the framework of the PRIN project "Engineering and biofunctionalization of scaffolds for tissue engineering" (project no. 20089CWS4C_003) is gratefully acknowledged.

Notes and references

1 (*a*) S. Sengupta and R. Sasisekharan, *Br. J. Cancer*, 2007, **96**, 1315–1319; (*b*) V. P. Torchilin, *Adv. Drug Delivery Rev.*, 2006, **58**, 1532–1555; (*c*) M. Ferrari, *Curr. Opin. Chem. Biol.*, 2005, **9**, 343–346; (*d*) M. Ferrari, *Nat. Rev. Cancer*, 2005, **5**, 161–171; (*e*) S. Kommareddy, S. B. Tiwari and M. M. Amiji, *Technol. Cancer Res. Treat.*, 2005, **4**, 615–625.

2 P. Ball, *The Self-made Tapestry: Pattern Formation in Nature*, Oxford University Press, New York, 1999.

3 For recent reviews on this subject see (*a*) P. K. Dhal, S. C. Polomoscanik, L. Z. Avila, S. R. Holmes-Farley and R. J. Miller, *Adv. Drug Delivery Rev.*, 2009, **61**, 1121–1130; (*b*) R. Gaspar and R. Duncan, *Adv. Drug Delivery Rev.*, 2009, **61**, 1220–1231; (*c*) X. Hu and X. Jing, *Expert Opin. Drug Delivery*, 2009, **6**, 1079–1090; (*d*) C. Khemtong, C. W. Kessinger and J. Gao, *Chem. Commun.*, 2009, 3497–3510; (*e*) M. Belting and A. Wittrup, *Mol. Biotechnol.*, 2009, **43**, 89–94; (*f*) J. Venugopal, M. P. Prabhakaran, S. Low, A. T. Choon, G. Deepika, V. R. Dev and S. Ramakrishna, *Curr. Pharm. Des.*, 2009, **15**, 1799–1808; (*g*) R. Singh and R, J. W. Lillard Jr, *Exp. Mol. Pathol.*, 2009, **86**, 215–223; (*h*) E. Soussan, S. Cassel, M. Blanzat and I. Rico-Lattes, *Angew. Chem., Int. Ed.*, 2009, **48**, 274–288; (*i*) M. A. Mintzer and E. E. Simanek, *Chem. Rev.*, 2009, **109**, 259–302; (*j*) M. C. Branco and J. P. Schneider, *Acta Biomater.*, 2009, **5**, 817–831; (*k*) S. Kim, J. H. Kim, O. Jeon, I. C. Kwon and K. Park, *Eur. J. Pharm. Biopharm.*, 2009, **71**, 420–430; (*l*) V. P. Torchilin, *Eur. J. Pharm. Biopharm.*, 2009, **71**, 431–444 and references therein.

4 (*a*) L. Leibler, *Macromolecules*, 1980, **13**, 1602–1617; (*b*) G. H. Fredrickson and L. Leibler, *Macromolecules*, 1989, **22**, 1238–1250; (*c*) F. S. Bates and G. H. Fredrickson, *Annu. Rev. Phys. Chem.*, 1990, **41**, 525–557; (*d*) S. B. Darling, *Prog. Polym. Sci.*, 2007, **32**, 1152–1204.

5 (*a*) S. K. Agrawal, N. Sanabria-Delong, G. N. Tew and S. R. Bhatia, *Langmuir*, 2008, **24**, 13148–13154; (*b*) S. K. Agrawal, N. Sanabria-Delong, G. N. Tew and S. R. Bhatia, *Macromolecules*, 2008, **41**(5), 1774–1784; (*c*) X. Garric, H. Garreau, M. Vert and J. P. Molès, *J. Mater. Sci.: Mater. Med.*, 2008, **19**, 1645–1651; (*d*) S. K. Agrawal, N. Sanabria-Delong, P. R. Jemian, G. N. Tew and S. R. Bhatia, *Langmuir*, 2007, **23**, 5039–5044; (*e*) W. C. Lee, Y. C. Li and I. M. Chu, *Macromol. Biosci.*, 2006, **6**, 846–854; (*f*) N. Sanabria-Delong, S. K. Agrawal, S. R. Bhatia and G. N. Tew, *Macromolecules*, 2007, **40**, 7864–7873; (*g*) S. K. Agrawal, N. Sanabria-Delong, J. M. Coburn, G. N. Tew and S. R. Bhatia, *J. Controlled Release*, 2006, **112**, 64–71; (*h*) T. Kissel, Y. Li and F. Unger, *Adv. Drug Delivery Rev.*, 2002, **54**, 99–134.

6 (*a*) G. Scocchi, P. Posocco, J.-W. Handgraaf, J. G. Fraaije, M. Fermeglia and S. Pricl, *Chem.–Eur. J.*, 2009, **15**, 7586–7592; (*b*) R. Toth, D.-J. Voorn, J.-W. Handgraaf, J. G. E. M. Fraaije, M. Fermeglia, S. Pricl and P. Posocco, *Macromolecules*, 2009, **42**, 8260–8270; (*c*) M. Fermeglia and S. Pricl, *Comput. Chem. Eng.*, 2009, **33**, 1701–1710; (*d*) M. Fermeglia and S. Pricl, in *IUTAM Symposium on Modelling Nanomaterials and Nanosystems*, ed. R. Pyrz and R. C. Rauhe, Springer-Verlag, Berlin, 2009, pp. 261–270; (*e*) M. Maly, P. Posocco, S. Pricl and M. Fermeglia, *Ind. Eng. Chem. Res.*, 2008, **47**, 5023–5038; (*f*) P. Cosoli, G. Scocchi, S. Pricl and M. Fermeglia, *Microporous Mesoporous Mater.*, 2008, **107**, 169–179; (*g*) G. Scocchi, P. Posocco, M. Fermeglia and S. Pricl, *J. Phys. Chem. B*, 2007, **111**, 2143–2151; (*h*) S. Pricl, M. Ferrone, M. Fermeglia, F. Amato, C. Cosentino, M. M. Cheng, R. Walczak and M. Ferrari, *Biomed. Microdevices*, 2006, **8**, 277–290; (*i*) F. Amato, C. Cosentino, S. Pricl, M. Ferrone, M. Fermeglia, M. M. Cheng, R. Walczak and M. Ferrari, *Biomed. Microdevices*, 2006, **8**, 291–298.

7 (*a*) P. J. Hoogerbrugge and J. M. V. A. Koelman, *Europhys. Lett.*, 1992, **19**, 155–160; (*b*) P. Español and P. B. Warren, *Europhys. Lett.*, 1995, **30**, 191–196; (*c*) R. D. Groot and P. B. Warren, *J. Chem. Phys.*, 1997, **107**, 4423–4435.

8 (*a*) A. Halperin, *Macromolecules*, 1987, **20**, 2943–2946; (*b*) R. Nagarajan and K. Ganesh, *Macromolecules*, 1989, **22**, 4312–4325; (*c*) R. Nagarajan and K. Ganesh, *J. Chem. Phys.*, 1989, **90**, 5843–5856; (*d*) E. B. Zhulina, M. Adam, I. LaRue, S. S. Sheiko and M. Rubinstein, *Macromolecules*, 2005, **38**, 5330–5351.

9 K. Devanand and J. C. Selser, *Macromolecules*, 1991, **24**, 5943–5947.

10 G. J. Fleer, M. A. Cohen Stuart, J. M. H. M. Scheutjens, T. Cosgrove, B. Vincent. *Polymers at Interfaces*, Chapman & Hall, Glasgow, U.K., 1993.

11 (*a*) S. A. Hagan, A. G. A. Coombes, M. C. Garnett, S. E. Dunn, M. C. Davies, L. Illum, S. S. Davis, S. E. Harding, S. Purkiss and P. R. Gellert, *Langmuir*, 1996, **12**, 2153–2161; (*b*) T. Riley, T. Govender, S. Stolnik, C. D. Xiong, M. C. Garnett, L. Illum and S. S. Davis, *Colloids Surf., B*, 1999, **16**, 147–159; (*c*) T. Govender, T. Riley, T. Ehtezazi, M. C. Garnett, S. Stolnik, L. Illum and S. S. Davis, *Int. J. Pharm.*, 2000, **199**, 95–110; (*d*) T. Riley, S. Stolnik, C. R. Heald, C. D. Xiong, M. C. Garnett, L. Illum, S. S. Davis, S. C. Purkiss, R. J. Barlow and P. R. Gellert, *Langmuir*, 2001, **17**, 3168–3174; (*e*) C. R. Heald, S. Stolnik, K. S. Kujawinski, C. de Matteis, M. C. Garnett, L. Illum, S. S. Davis, S. C. Purkiss, R. J. Barlow and P. R. Gellert, *Langmuir*, 2002, **18**, 3669–3675; (*f*) T. Riley, S. Stolnik, M. C. Garnett, L. Illum, S. S. Davis, P. Taylor and Th. F. Tadros, *Langmuir*, 2002, **18**, 7663–7668; (*g*) T. Riley, C. R. Heald, S. Stolnik, M. C. Garnett, L. Illum, S. S. Davis, S. M. King, R. K. Heenan, S. C. Purkiss, R. J. Barlow, P. R. Gellert and C. Washington, *Langmuir*, 2003, **19**, 8428–8435; (*h*) E. Pierri and K. Avgoustakis, *J. Biomed. Mater. Res., Part A*, 2005, **75a**, 639–647.

12 M. Ripoll, M. H. Ernst and P. Español, *J. Chem. Phys.*, 2001, **115**, 7271–7284.

13 M. A. Horsch, Z. Zhang, C. R. Iacovella and S. C. Glotzer, *J. Chem. Phys.*, 2004, **121**, 11455–11462.

14 R. D. Groot and T. J. Madden, *J. Chem. Phys.*, 1998, **108**, 8713–8724.

15 D. N. Theodorou and U. W. Suter, *Macromolecules*, 1986, **19**, 139–154.

16 For the application of our MDSA protocol see, for instance (*a*) A. Carta, G. Loriga, S. Piras, G. Paglietti, P. La Colla, G. Collu, M. A. Piano, R. Loddo, M. Ferrone, M. Fermeglia and S. Pricl, *Med. Chem.*, 2006, **2**, 577–589; (*b*) E. Banfi, G. Scialino, D. Zampieri, M. G. Mamolo, L. Vio, M. Ferrone, M. Fermeglia, M. S. Paneni and S. Pricl, *J. Antimicrob. Chemother.*, 2006, **58**, 76–84; (*c*) P. Posocco, M. Ferrone, M. Fermeglia and S. Pricl, *Macromolecules*, 2007, **40**, 2257–2266; (*d*) A. Carta, M. Loriga, S. Piras, G. Paglietti, M. Ferrone, M. Fermeglia, S. Pricl, P. La Colla, G. Collu, T. Sanna and R. Loddo, *Med. Chem.*, 2007, **3**, 520–532; (*e*) D. Zampieri, M. G. Mamolo, L. Vio, E. Banfi, G. Scialino, M. Fermeglia, M. Ferrone and S. Pricl, *Bioorg. Med. Chem.*, 2007, **15**, 7444–7458; (*f*) M. Mazzei, E. Nieddu, M. Miele, A. Balbi, M. Ferrone, M. Fermeglia, M. T. Mazzei, S. Pricl, P. La Colla, F. Marongiu, C. Ibba and R. Loddo, *Bioorg. Med. Chem.*, 2008, **16**, 2591–2605; (*g*) D. Zampieri, M. G. Mamolo, E. Laurini, M. Fermeglia, P. Posocco, S. Pricl, E. Banfi, G. Scialino and

L. Vio, *Bioorg. Med. Chem.*, 2009, **17**, 4693–4707; (*h*) Tonelli, I. Vazzana, B. Tasso, V. Boido, F. Sparatore, M. Fermeglia, M. S. Paneni, P. Posocco, S. Pricl, P. La Colla, C. Ibba, B. Secci, G. Collu and R. Loddo, *Bioorg. Med. Chem.*, 2009, **17**, 4425–4440, and references therein.
17 Y. Li and W. A. Goddard III, *Macromolecules*, 2002, **35**, 8440–8455.
18 (*a*) J. Blomqvist, L. Ahjopalo, B. Mannfors and L.-O. Pietilä, *THEOCHEM*, 1999, **488**, 247–262; (*b*) J. Blomqvist, B. Mannfors and L.-O. Pietilä, *THEOCHEM*, 2000, **531**, 359–374.
19 (*a*) J. Blomqvist, L.-O. Pietilä and B. Mannfors, *Polymer*, 2001, **42**, 109–116; (*b*) J. Blomqvist, *Polymer*, 2001, **42**, 3515–3521.
20 F. Müller-Plathe, *ChemPhysChem*, 2002, **3**, 754–769.